Transmissibility Corrections and Grid Control for Shale Gas Numerical Simulation

Vincent Artus - Dorian Fructus

Abstract

In the context of shale gas production, the very low effective permeability of the formation leads to flowing conditions that are essentially transient. Even after months or years of production, the pressure drop remains mainly localized around the hydraulic fractures. Using an unstructured grid, finite-volume simulator, we show that the non-linear nature of the pressure field around horizontal wells with multiple hydraulic fractures can have a non-negligible impact on shale gas production forecasts.

We first show a very simple synthetic production example, with a purely linear PVT. In this case, standard (linear) transmissibility derivations overestimate the forecast after 10 years by 5%, compared to the analytical solution. We propose a new approach for transmissibility derivations, based on numerical integrations of source point solutions. Resulting transmissibility values account for the strong non-linearity of the pressure field in the vicinity of the fractures, and for fracture interferences. As a consequence, forecasts are significantly improved.

With a real gas PVT, non-linear effects become even more critical in the vicinity of the well. While analytical solutions only partially account for these effects, numerical simulations are more accurate, provided that the grid is fine enough. In order to reduce the computational cost, long-term simulations are usually performed on a coarser grid, with coarse transmissibility corrections obtained from near-well upscaling techniques. We show that even if near-well numerical upscaling is extremely robust for conventional problems, the choice of an optimal simulation grid size becomes essential for shale gas. A recently proposed automatic adjustment of the grid to the considered problem (including permeability and time resolution) is tested.

Introduction

Data history matching and production forecasting in shale gas context raises new challenges linked to the low-permeability, fully transient context. Recently, a complete workflow has been proposed and tested [1, 2]. As described in the cited papers, the workflow starts with the simplest methods, such as diagnostic plots and straight line analysis, and progressively includes more sophisticated models in order to account for increasing physical complexity. The last two main steps, and most advanced options of the workflow are:

- A transient, analytical model for horizontal wells with multiple hydraulic fractures. This model accounts for interferences between hydraulic fractures and allows for various fracture flow models (infinite conductivity, finite conductivity or uniform flux). However, it does not account for the non-linearity of gas PVT properties. Also, it cannot account for advance effects such as desorption, multiphase flow, or unconsolidation…

- A numerical model including a large range of physical complexity, such as non-linear PVT, complex fractures geometry, heterogeneity, non-consolidation and desorption. Although this model is the one that should ultimately be used for forecasting, it potentially involves so many unknowns that it should be used at the end of the analysis process only, i.e. once the main unknowns have been significantly constrained by diagnostic tools and analytical interpretation.

At each step of the workflow, the results of the last analysis are used as a starting point for the next model, which includes additional physical effects. At each stage, results and forecasts are checked, and the validity/influence of any new sophistication can be analyzed in order to ensure proper update of the different parameters.

It is obvious that at each stage, the results of the different methods must be coherent in order to ensure the overall robustness of the complete analysis. In particular, under the same assumptions, different methods should give similar results.

The objective of this paper is to focus on the comparison between the analytical, multiple fractures horizontal well model and the numerical model, trying to explain and correct existing differences. We show that the transient, non-linear nature of the pressure field around fractures can challenge the classical assumptions of the numerical model. As a consequence, both the transmissibility derivations and the automatic gridding procedure were adapted.

This validation step under simplistic assumptions (simple PVT and geometry, no desorption, etc…) is essential to the integration of the numerical model in the workflow, i.e. just before adding further complexity. This should prevent tuning fudge parameters in the full-physics model to compensate for uncontrolled, purely numerical effects…

1. Pressure transient and non-linear effects

Reservoir data	
Initial Reservoir Pressure, psia	5000
Reservoir temperature, ºF	112
Reservoir radius, ft	10,000
Net pay, ft	100
Porosity, %	10
Swi, %	0
Gas specific gravity	0.65
Well data	
Horizontal well length, ft	4000
Horizontal well position	centered
Horizontal well skin factor	0
Number of Fractures	20
Fractures half-length Xf, ft	250
Fractures position	centered
Fractures penetration	full
Fractures conductivity Fc, md.ft	1000
Well flowing pressure, psia	250
Completion type	cased hole

Table 1 – Reservoir and well properties

Let us consider a simple reservoir, as described in Table 1 and Figures 1 and 2. For the numerical model, we use a finite-difference simulator with a Voronoi grid, allowing smooth grid refinement close to the fractures. By default, the size of the finest cells is automatically set to a couple of times the width of the fracture and a default cell size progression ratio of 1.4 is applied as one moves away from the fracture, until the constant size 'back grid' cells (hexagons) are reached.
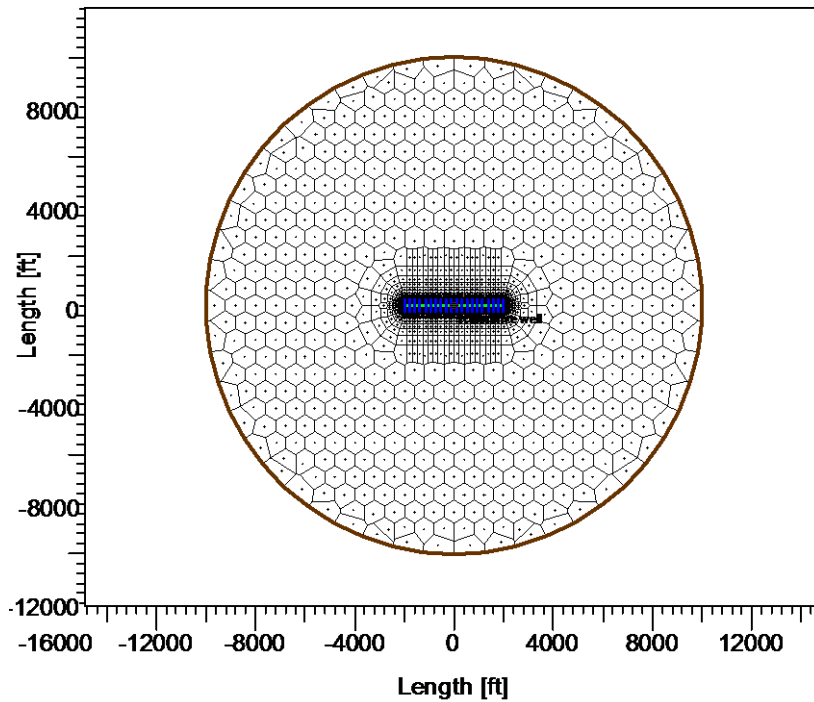
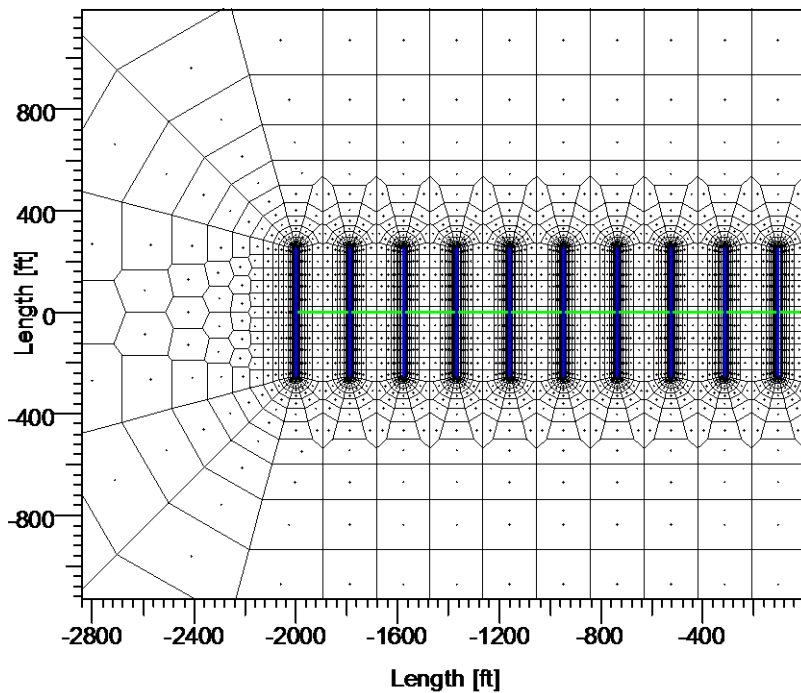*Figure 1 – Voronoi grid for the reservoir described in Table 1.*

Figure 2 – Voronoi grid (close-up on hydraulic fractures)

As a starting point, let us further assume that the gas PVT has constant viscosity and compressibility, and that the permeability is homogeneous, with a conventional value k=30 mD.

The reservoir is produced at constant well pressure P=250 psia for ten years. As can be seen from figures 3 and 4, the match between the analytical model and the numerical model is excellent, both for early-time transient analysis and long-term forecasting.
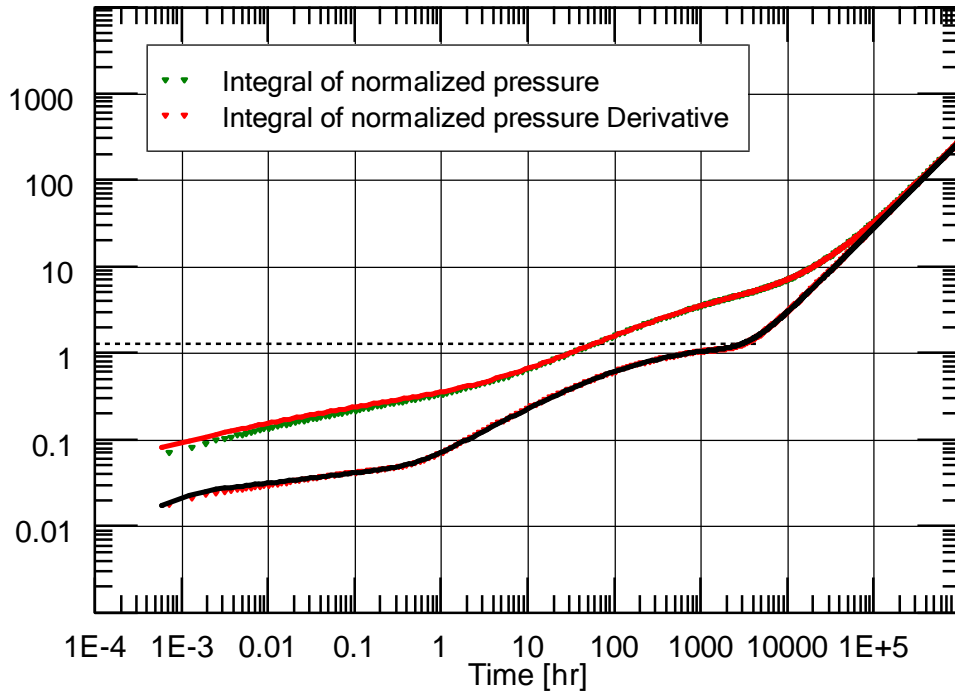
*Figure 3 – Comparison of pressure and pressure derivative curves
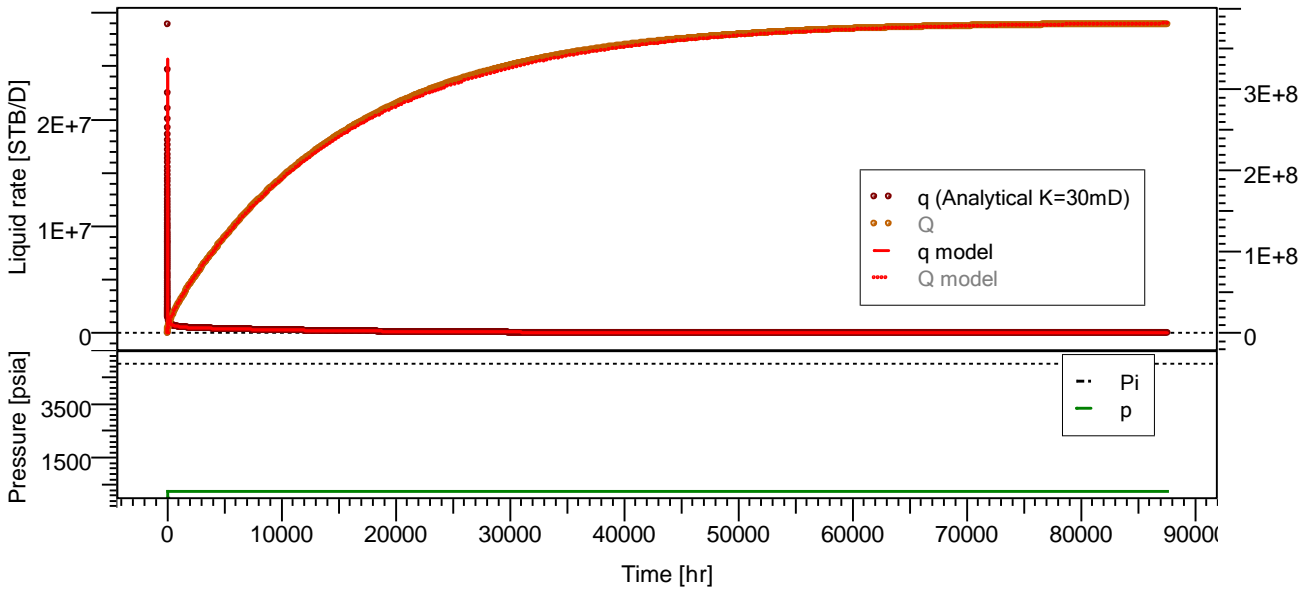between analytical (markers) and numerical (continuous lines) results. k=30 mD.*

Figure 4 – Comparison of analytical (markers) and numerical ('model') forecasts. k=30 mD.

Let us now reduce the permeability of the medium, so that k=1e-4 mD.

It is worth recalling here that reducing k by several order of magnitudes is quite similar to zooming on short times with a conventional case. Small k will hence amplify the importance of transient effects, in a zone where most numerical errors typically appear. Indeed, on figures 5 and 6, we now see that several discrepancies arise, both at early time (loglog plot figure 5) and at late time (production forecast, figure 6).

First, as visible from Figure 5, the early-time behavior is completely lost. Part of this discrepancy is explained by the compressibility of the fluid inside the fracture, which is accounted for by the numerical model only. However, as was already noticed in [1], the derivative curve obtained with the standard grid shows a purely numerical, 'double-porosity looking' effect. This has to be related to the size of the first rings of cells around the fractures. Although the standard size was quite sufficient to capture the early-time behavior for a conventional range of permeability values, we see that it cannot be set irrespectively of the permeability field in nano to micro Darcy permeability formations. Indeed, reducing the grid size to millimeter scale in the vicinity of the fracture solves the problem (ultra-fine grid in Figure 5). A practical objective of this study is to find the best resolution depending on the context, without having to systematically use the finest grid. This will be developed in section 5, dedicated to grid refinement control.
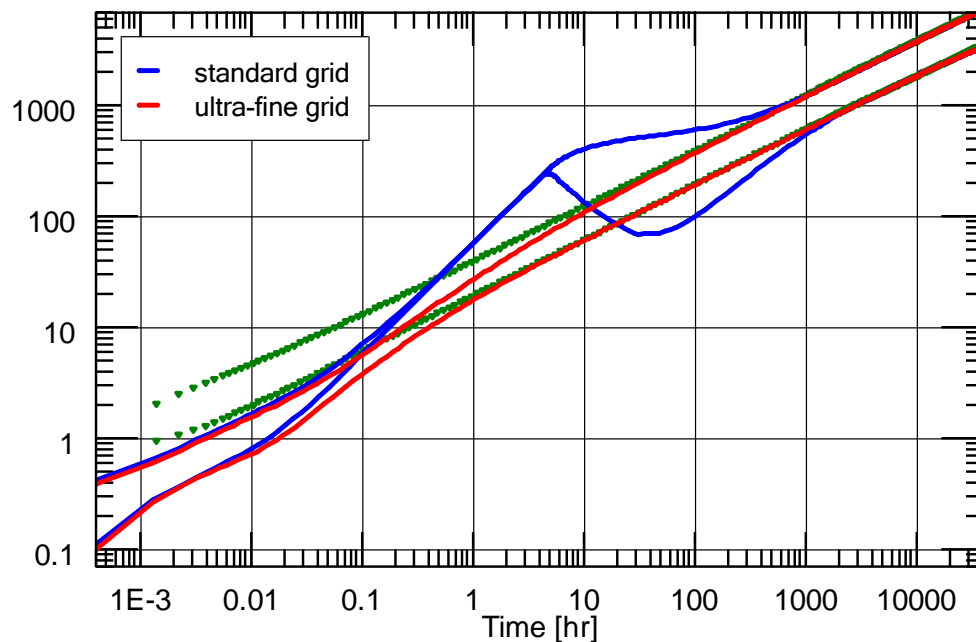

*Figure 5 – Comparison of pressure and pressure derivative curves
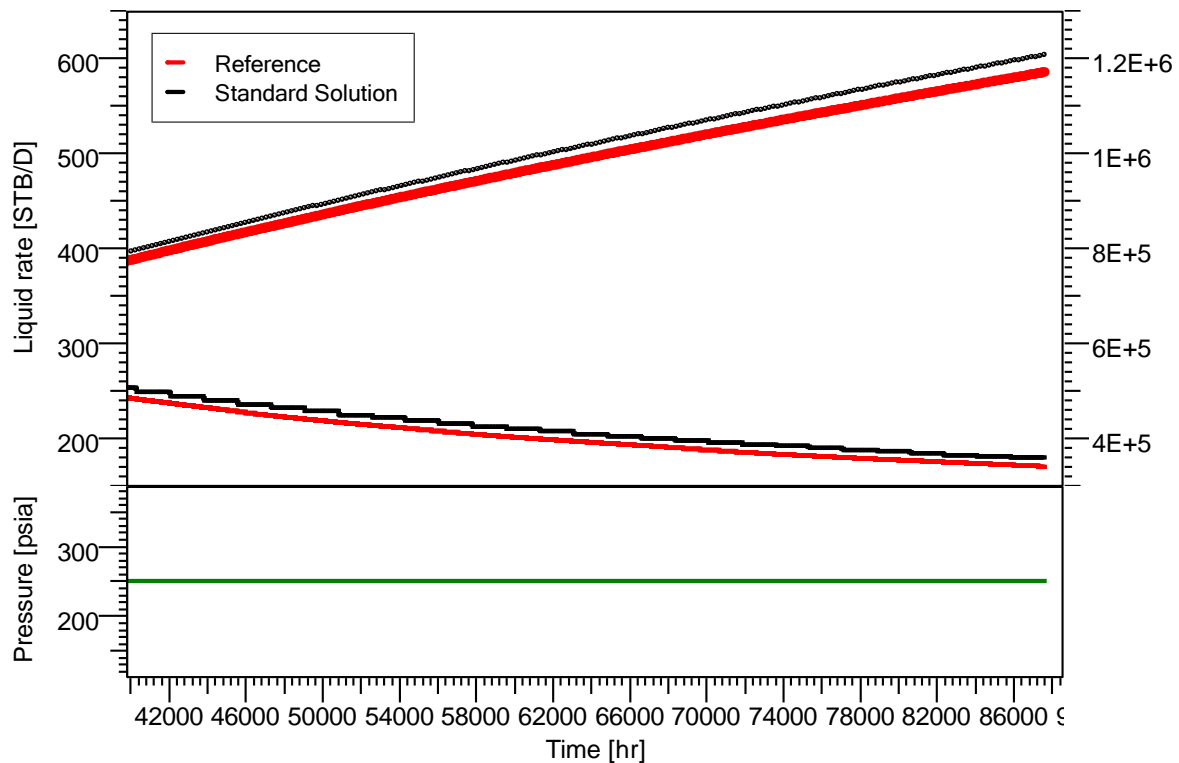between analytical (markers) and numerical (continuous lines) results. k=1E-4 mD.*

Figure 6 – Comparison of analytical (markers) and numerical ('model') forecasts. k=1E-4 mD.

Second, the long-term forecasts can be significantly deviating (Figure 6). After 10 years, the cumulative predicted by the numerical model can be up to 5% greater than the analytical prediction in some cases. This is related to the strong non-linear behavior of the pressure field in the vicinity of the fractures. As a consequence of this effect, the standard linear assumption behind transmissibility derivations cannot hold anymore, although the grid is very fine and K-orthogonal. This phenomenon was negligible with a conventional permeability. With shale gas, however, the pressure drop remains localized in the vicinity of the fractures even after years of production, and non-linear effects cannot be neglected anymore.

Finally, let us consider the non-linear nature of gas PVT properties. As previously noticed in [1], the high compressibility of the gas in the vicinity of the fractures increases the overall productivity. This effect can be accounted for by the numerical model only. Indeed, by assuming a constant $\mu_g.c_g$ product (gas viscosity $\times$ compressibility), analytical calculations systematically underestimate the productivity in this context (Figure 7), leading to significantly lower cumulatives. However, in order to fully rely on the numerical answer, we must ensure that the numerical model correctly captures the variations of cg and µg close to the fractures, i.e. that the grid is fine enough.
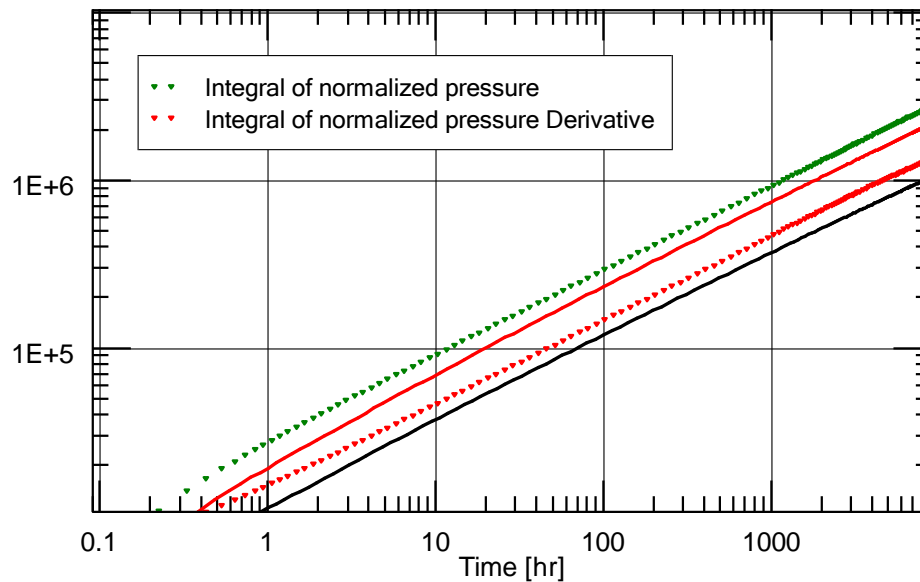
Figure 7 – Comparison of pressure and pressure derivative curves between analytical (markers) and numerical (continuous lines) results for a non-linear gas PVT. k=1E-4 mD.

As a consequence of these observations, we decided to develop a new transmissibility derivation algorithm, which should account for non-linear pressure effects and ultimately reduce the discrepancy between analytical and numerical results under similar assumptions. Furthermore, an automatic adjustment of the grid (through numerical upscaling) to the formation permeability and desired time-scale resolution was implemented, following the observations made in [3]. Its purpose is to solve the early-time deviation due to the resolution of the model, and better constrain the handling of gas compressibility in the vicinity of the fractures, when non-linear PVT is considered.

2. Transmissibility calculations

The problem of correctly modeling fluid flow in the vicinity of the well is a difficult task. This is due to the fact that the transmissibilities are computed based on the gridding geometry, assuming a predefined simple pressure behavior around each cell face. These derivations are usually made assuming linear, geometric or logarithmic pressure evolution away from the well and account for pressure variation on cell faces throughout simple geometrical correction. However, they do not account for pressure variation along the faces themselves. This usually leads to satisfactory results for standard well geometry. For complex 3D geometries, however, neglecting the complex variation of the pressure profile along the faces may lead to incorrect flow representation. In order to correctly model the flow in this region, local pressure variations have to be taken into account. This effect becomes predominant for low permeability problems, where pressure variations are locally very important.

Several authors have investigated this problem by means of simple analytical solutions. This is possible as long as the pressure field is 2D and is limited by simple well geometry. For complex 3D problems, if the fluid is assumed uncompressible, a potential solution has to be found numerically. Lee [4, 5] introduced a boundary integral representation for the pressure field around the wellbore and later used the slender body theory in order to correct the production index. A similar method was developed by Ding [6, 7] and extended to the near wellbore region to correct well index and the grid transmissibilities in the near wellbore region. Their integral representation was based on simple kernels. In this paper, we present a methodology using an integral representation of the potential field based on elementary Green's function surfaces that are given analytically. We derive the corresponding analytical kernels for each surface type. The producing fracture surfaces are then discretized and elementary surfaces

contributions are distributed over each surface. This leads to a global linear system involving interaction coefficients that has to be solved to insure the boundary condition at the producing surfaces. If the problem at hand can be reduced to 2D (fully perforating vertical fracture for example), an analytical solution to the corresponding system is used, leading to a very fast transmissibility calculations scheme.

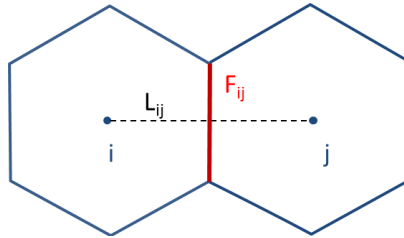Let us start by considering two adjacent cells of a k-orthogonal grid, in a homogenous reservoir (Figure 8).

Figure 8 – Two adjacent cells of a k-orthogonal grid

The flux between the two cells is classically written as a function of the pressure drop through the use of a constant transmissibility:

$$Q_{ij} = \frac{1}{\mu} T_{ij} \left(\overline{P}_i - \overline{P}_j \right)$$

where $\overline{P}_i$ and $\overline{P}_j$ are the average pressures in each cell.

The usual linear assumption on the pressure field leads to the following standard expression for transmissibility:

$$T_{ij} = \frac{k \cdot F_{ij}}{L_{ij}}$$

Above, F_{ij} is the surface of the face between the two cells, and L_{ij} is the distance between the two nodes.

If the pressure field cannot be considered linear in the two cells, another expression has to be found. Let us express the average pressure in each cell (of volume v_i) :

$$\overline{P}_i = 1/v_i \cdot \iiint_{Ci} P dv$$

Alternatively, Darcy's law gives:

$$Q_{ij} = \iint_{Fij} \vec{u} \cdot d\vec{S} = \frac{-k}{\mu} \cdot \iint_{Fij} \nabla P \cdot d\vec{S}$$

The transmissibility can hence be expressed as:

$$T_{ij} = -k \frac{\iint_{Fij} \nabla P \cdot d\vec{S}}{1/v_i \cdot \iiint_{Ci} P dv - 1/v_j \cdot \iiint_{Cj} P dv}$$

And the well index is given by:

$$WI = -k \frac{\iint\limits_{Fiw} \nabla P \cdot d\vec{S}}{1/v_i \cdot \iiint\limits_{Ci} Pdv - Pw + S \cdot \iint\limits_{Fiw} \nabla P \cdot d\vec{S}}$$

If the fluid compressibility is further neglected, the pressure field becomes harmonic and can be expressed in terms of Greens function representation. For a source point located at $\vec{x}_s$, we define a free space function by $G^0(\vec{x};\vec{x}_s) = \lambda(\vec{x}_s)/\|\vec{x} - \vec{x}_s\|$. Assuming a distribution of source points, the free space function can be integrated to obtain the resulting potential field:

$$\phi(\vec{x}) = \int\limits_{S} G^0(\vec{x};\vec{x}_s)d\vec{x}_s$$

This field being directly proportional to the uncompressible pressure field, the formulae for transmissibility and well index can be used directly with the potential in place of the pressure.

3. Solution Procedure

The evaluation of the potential field is done differently depending on the complexity of the problem. If the problem at hand is two-dimensional (fully perforating fractures for example), an analytical solution can be found by conformal mapping techniques. When the problem becomes three-dimensional, a numerical evaluation procedure must be used to evaluate the potential function. In this case the surface is discretized in terms of elementary surfaces and the linearity of the problem at hand allows for direct superposition of individual contribution to obtain the resulting potential field.

Another difficulty arises from the required boundary condition at the producing surfaces: the superposition of singularity distribution with the same strength leads to a solution equivalent to the uniform flux solution, i.e. the pressure is not constant along the producing area, on each elementary surface. In order to obtain a constant boundary pressure condition (infinite conductivity fracture for example), a numerical procedure must be involved to compute distribution strength on each elementary surface.

For two-dimensional problems, conformal mapping techniques give closed form solutions for given geometry and boundary conditions. In the present case, we can consider the potential between co-focal ellipses with a degenerate inner ellipse given by:

$$\phi(x, y) = \ln\left(\frac{a + b}{X_f}\right)$$, where X_f is the half segment length and $\frac{x^2}{a^2} + \frac{y^2}{b^2} = 1$

$$b = \sqrt{\frac{1}{2}\left[\left(x^2 + y^2 - X_f^2\right) + \sqrt{\left(x^2 + y^2 - X_f^2\right)^2 + 4y^2 X_f^2}\right]}$$, and $a = \sqrt{X_f^2 - b^2}$

This solution can be readily used for fully perforating fractures. Note however that in multi-fracture cases the superposition of an array of such solutions would lead to a solution that would not fulfil the constant pressure condition at the fracture faces. In this case, the potential field is built from superposition of local potential fields (no interferences).

For complex three-dimensional problems, such as slanted wells or partially penetrating fractures, the two-dimensional solution cannot be used, and closed form three-dimensional solutions are limited to very simple geometries.

The source configuration, composed of either well segments or individual fractures, is subdivided into subsections onto which a constant source distribution is considered (Figure 9):
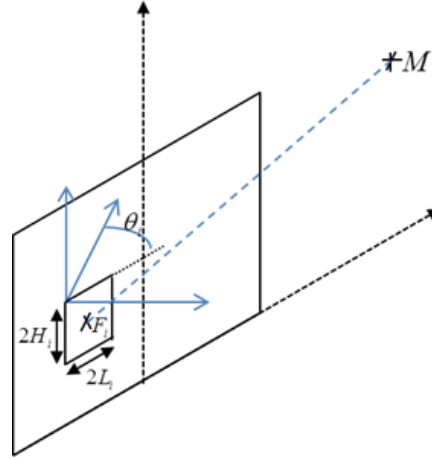

Figure 9 – Fracture description

We have:

$$\phi(M) = \sum_i \beta_i \cdot \phi_u^{rec}(M, F_i, L_i, H_i, \theta_i)$$

Where ϕ_u^{rec} is the panel unitary source solution as given in Appendix A. Assuming vertical fractures, the two first images are accounted for by super-imposing the corresponding solutions:

$$\phi(M) = \sum_i \beta_i \cdot \left\{ \phi_u^{rec}(M, F_i, L_i, H_i, \theta_i) + \phi_u^{rec}(M, F_i^U, L_i, H_i, \theta_i) + \phi_u^{rec}(M, F_i^D, L_i, H_i, \theta_i) \right\}$$

With F_i^U and F_i^D corresponding to the images of the section center with respect of the upper and lower bound (horizon) respectively.

The determination of the β_i coefficients is done differently depending on the boundary conditions insured at the producing surfaces. If a uniform flux condition is desired, these coefficients are all set to unity resulting in a varying potential along the producing surface. In this case the segmentation is reduced to a single element and the computation is straightforward. In the more complex case where a constant potential at the surface is required, corresponding to the infinite conductivity condition, the equality of potential between a set of points chosen at the center of each subsection is expressed. This results in a linear system that has to be solved in order to obtain these coefficients.

A similar technique is employed in the case of wells with multiple segments and/or slanted geometry where the unitary panel solution ϕ_u^{rec} is replaced by unitary segment solution ϕ_u^{Seg} as given in Appendix A.

4. Numerical examples

In order to properly assess the validity of the proposed methodology, we consider four examples with fractures in low permeability medium and restrict the simulation to the linear PVT case. In this context, we can compare to analytical solutions computed using Ozkan and Raghavan methodology [8].

Case a) 2D Single Fracture constant pressure production

We first consider a case with a single fracture (see parameters on Table 2) which has a complete penetration in a homogeneous layer. In this case the potential is purely 2D. The well is set to produce at constant bottom-hole pressure for 27 years.

Reservoir data	
Initial Reservoir Pressure, psia	5000
Net pay, ft	100
Porosity, %	10
Permeability, mD	1E-3
Well data	
Number of Fractures	1
Fractures half-length Xf, ft	400
Fractures position	centered
Fractures penetration	full
Fractures conductivity Fc, md.ft	infinite
Production duration, years	27

Table 2 – Reservoir and well properties

Figure 10 displays the production rate and cumulative production obtained with and without the proposed transmissibility corrections, compared to that obtained from the reference solution. Figure 11 displays the cumulative relative production error with and without transmissibility corrections.

It is clear that the solution obtained without transmissibility corrections leads to an increasing error with time (we extended it to 100 years and obtained 5% error on the standard cumulative). On the contrary, the proposed solution leads to a bounded error, which in this case is always lower than 1 percent in terms of cumulative production.
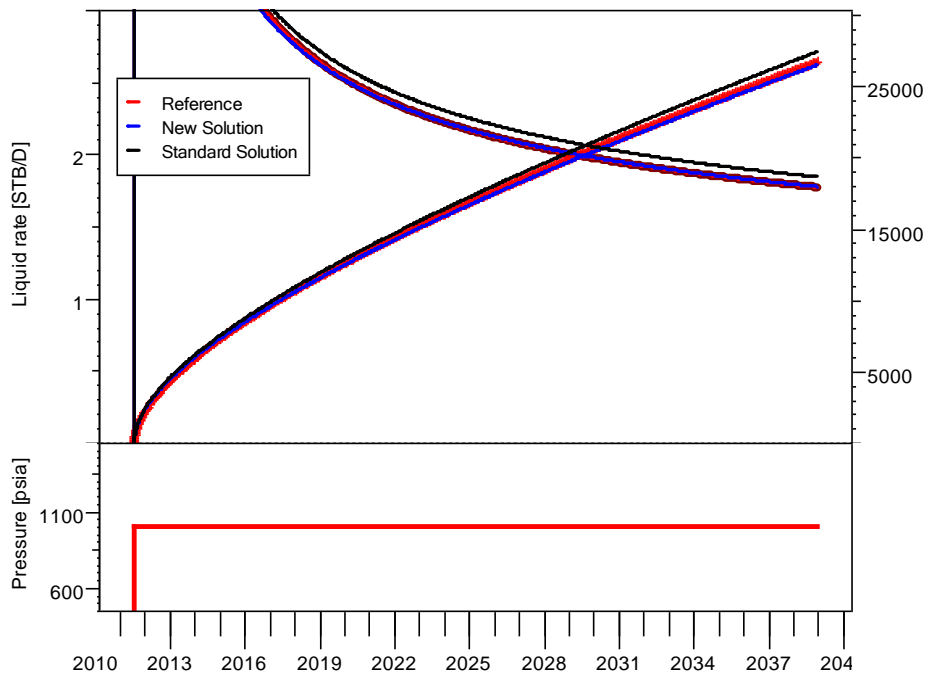
Figure 10 – Cumulative production with and without transmissibility corrections versus reference solution (red).
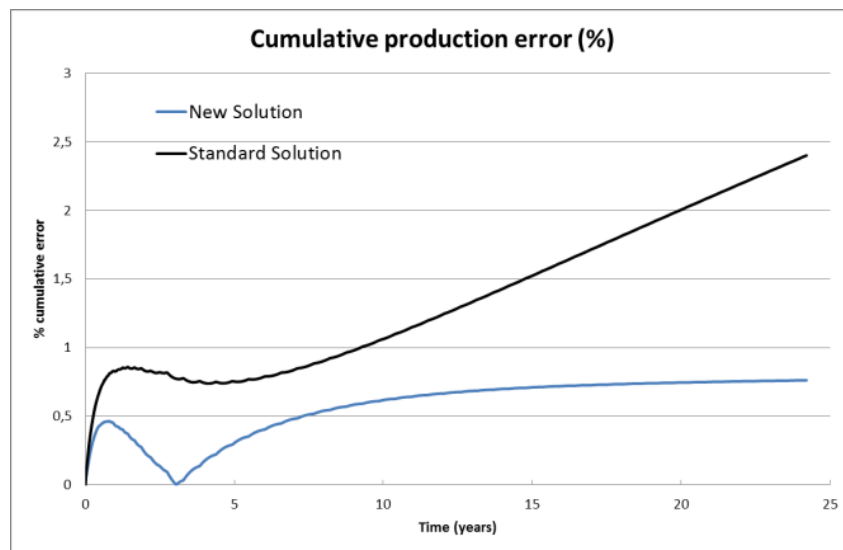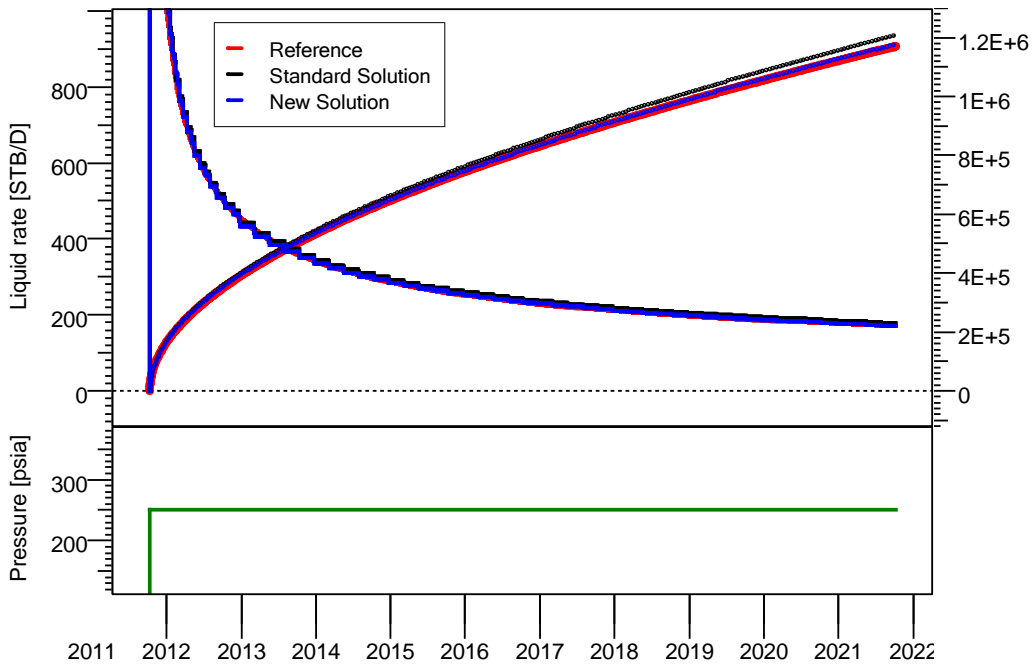

Figure 11 – Cumulative production error (relative to reference cumulative) with and without transmissibility corrections versus time.

Case b) 2D Multi-fracture production

Next, we consider again the example of Section 1, summarized in Table 1, with k=1E-4 mD. It is a 20 fractures case with complete penetration in a homogeneous layer. In this case, the potential is still 2D.

The well is set to produce at constant bottom-hole pressure for 10 years. Figures 12 and 13 display the cumulative production obtained analytically ('reference') and numerically, with and without correction.

It is worth mentioning that this case exhibits strong interferences between fractures during production. Even in this context, we see that our solution remains very robust.

Figure 12 – Cumulative production with and without transmissibility corrections versus reference solution (thick red line).
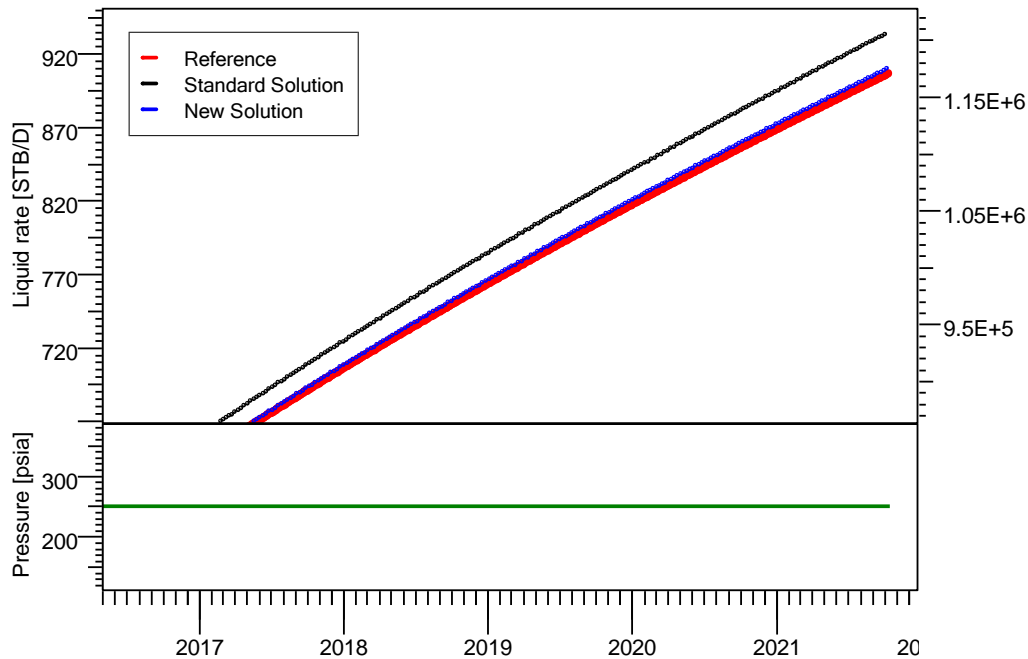

Figure 13 – Cumulative production with and without transmissibility corrections versus reference solution (thick red line).

Figure 14 displays the cumulative relative production error with and without transmissibility corrections. The solution obtained without transmissibility corrections leads as before to an increasing error with time, reaching 3 percent after 10 years of production. The proposed solution leads to a bounded error which is in this case is lower than 0.5 percent in terms of cumulative production.
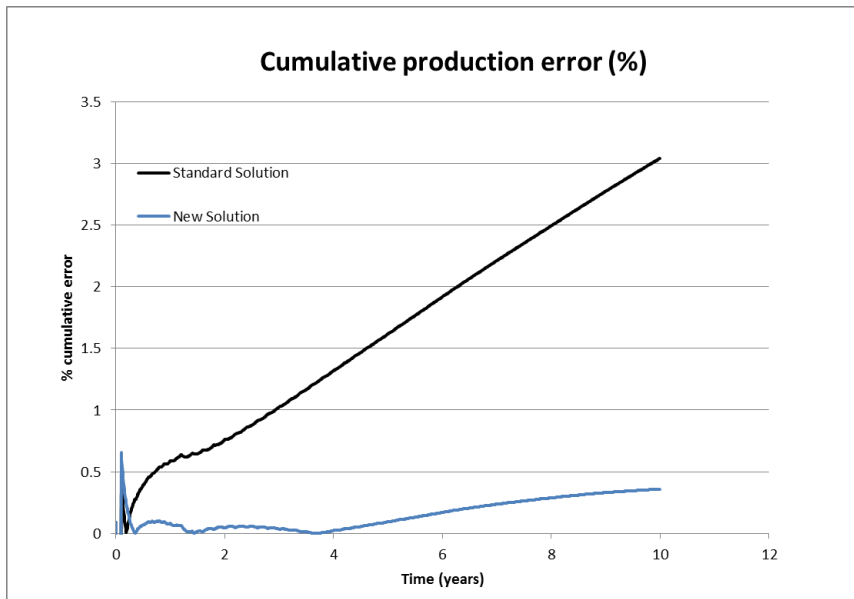
*Figure 14 – Cumulative production error (relative to reference cumulative)
with and without transmissibility corrections versus time.*

Case c) 3D Limited height single fracture constant pressure production

We now consider a 3D problem with a single limited height fracture (Table 3). Figures 15 and 16 display the production rate and cumulative production as well as the cumulative relative production error with and without transmissibility corrections. As for the 2D problems, the new corrections lead to a clear improvement in this case.

Reservoir data	
Initial Reservoir Pressure, psia	5000
Net pay, ft	100
Porosity, %	10
Permeability, mD	1E-3
Well data	
Number of Fractures	1
Fractures half-length Xf, ft	400
Fractures position	centered
Fractures penetration, ft	40
Fractures top depth, ft	20
Fractures conductivity Fc, md.ft	infinite
Production duration, years	27

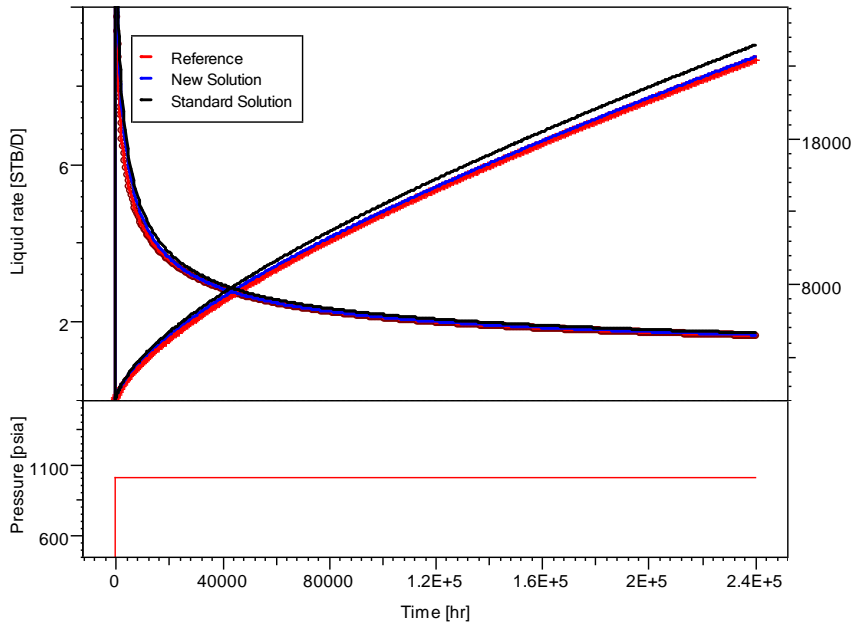*Table 3 – Reservoir and well properties*

Figure 15 – Cumulative production with and without transmissibility corrections versus reference solution (thick red line).
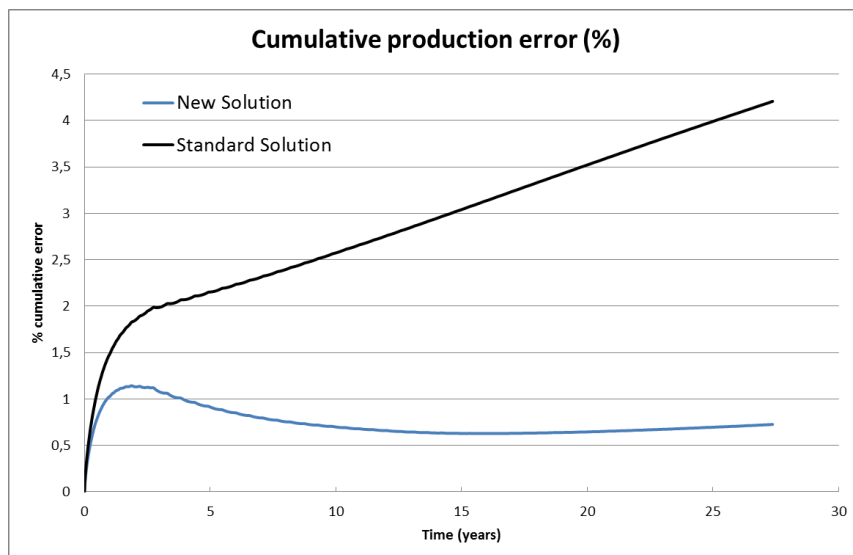

Figure 16 – Cumulative production error (relative to final reference cumulative) with and without transmissibility corrections versus time.

Case d) 3D Limited height multi-fracture constant pressure production

We finally consider a complex 3D problem with a limited height multi-fractures case (Table 4). Figure 17 displays the truncated numerical grid in this case where the colors correspond to the magnitude of the calculated potential.

Figures 18 and 29 display the production rate and cumulative production as well as the cumulative relative production error with and without transmissibility corrections in this case. As for the previous examples, the new corrections lead to a clear improvement while the standard solution shows an error on the cumulative production which is increasing with time.

Reservoir data	
Initial Reservoir Pressure, psia	5000
Net pay, ft	100
Porosity, %	10
Permeability, mD	1E-3
Well data	
Well length (ft)	2000
Number of Fractures	5
Fractures half-length Xf, ft	400
Fractures position	centered
Fractures penetration, ft	40
Fractures top depth, ft	10
Fractures conductivity Fc, md.ft	infinite
Production duration, years	27
Well completion type	cased hole

Table 4 – Reservoir and well properties
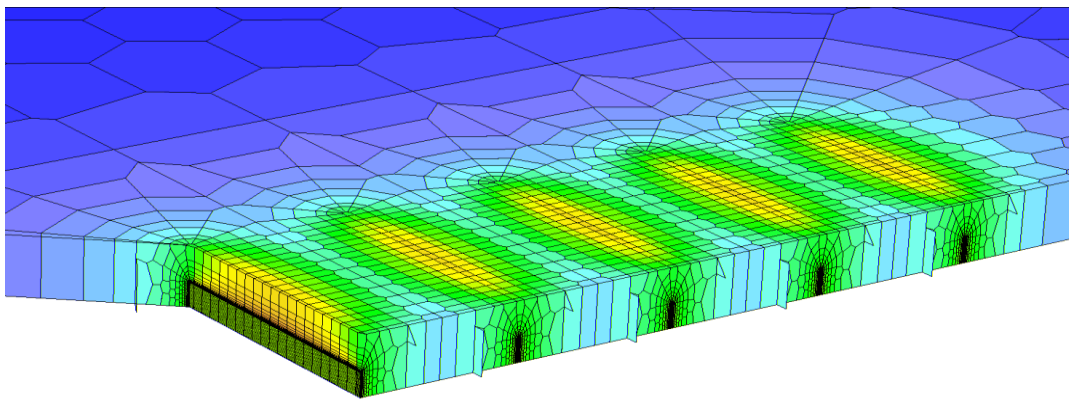
Figure 17 – Truncated numerical grid. The colors correspond to the calculated potential.
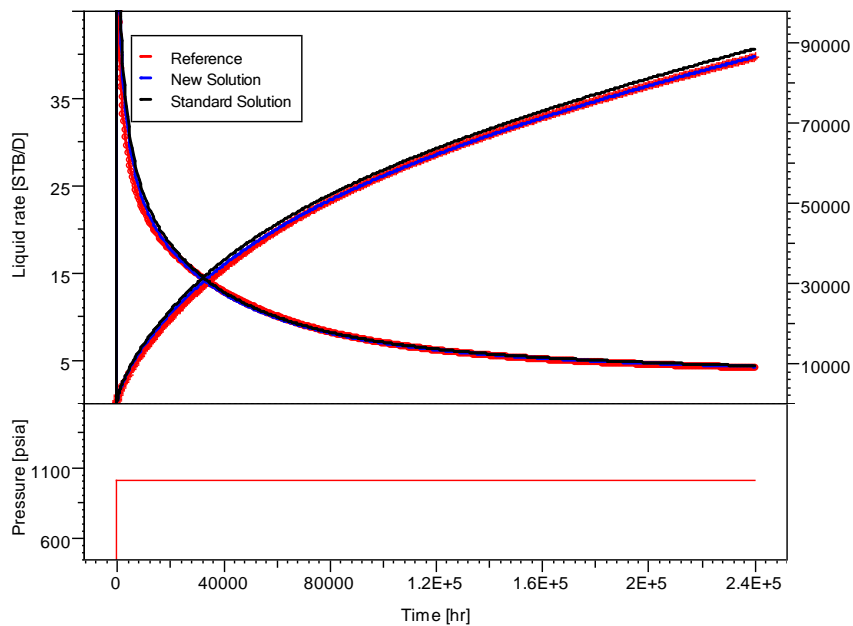

Figure 18 – Cumulative production with and without transmissibility corrections versus reference solution (thick red line).
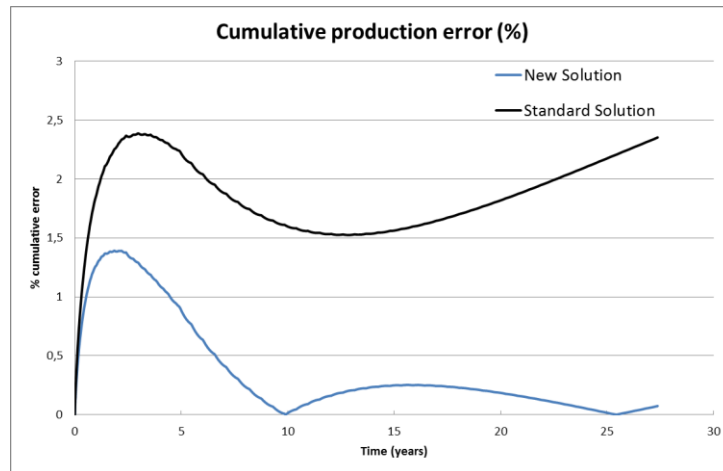
Figure 19 – Cumulative production error (relative to final reference cumulative)
with and without transmissibility corrections versus time.

5. Grid refinement control

Analysing Figure 5, we saw that the extremely low value of the permeability in shale gas context enforces the use of a very fine grid in order to correctly simulate early-time transient effects. In many cases, however, the early-time behaviour is not essential to the interpretation and a coarser grid may be sufficient, as long as later time scales are correctly captured. This can be properly addressed with numerical near-well upscaling [9, 10].

Using this methodology, the well index and the transmissibility values of the coarse grid are corrected using the results of a steady-state, fine-grid simulation. Figure 20 shows the resulting cumulative obtained for various grid sizes, for the example of Table 1, with k=1e-4 mD and linear PVT. We see that the overall process is extremely robust, so forecasts match perfectly. Note that in this example, the gain on the number of cells is reached only by coarsening the size of the first rings of cells around the fractures (from millimetres to meters scale) without changing the back grid. Note that the excellent match at late-time is not a surprise since the original field was homogeneous. However, the overall procedure also gives very good results at late time, even with near-well heterogeneity.

On the loglog plot (Figure 21), we see that early times are lost after the upscaling process. This is logical: while the grid is coarsened, near-fracture cells become too large to capture transient effects correctly. We see that, however, after a given time which depends on the coarsening level, any curve nicely comes back on the derivative of the finest, reference simulation. What is important to notice here is that even for a mild coarsening level, the correct answer is captured only after 100 hr, because of the very low permeability. For a conventional permeability value, it would only be a matter of minutes even with a larger upscaling level. This raises a practical problem, as one would like to choose the best coarsening level depending on the desired time resolution of its analysis, i.e. without always simulating on the finest grid.
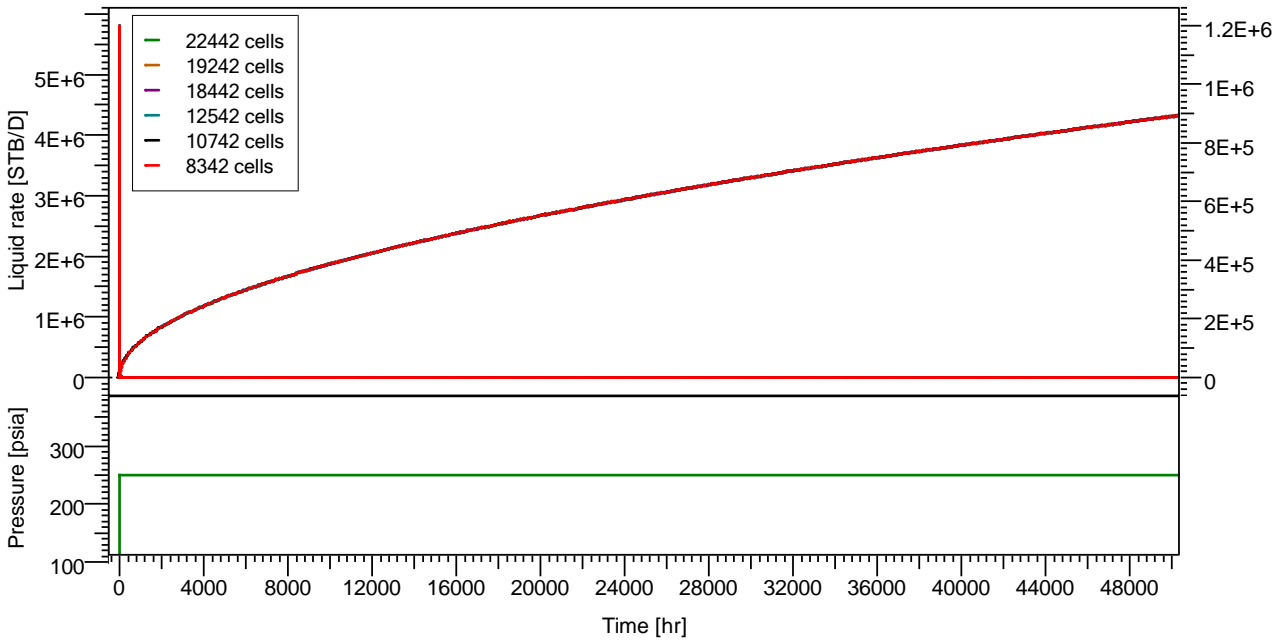
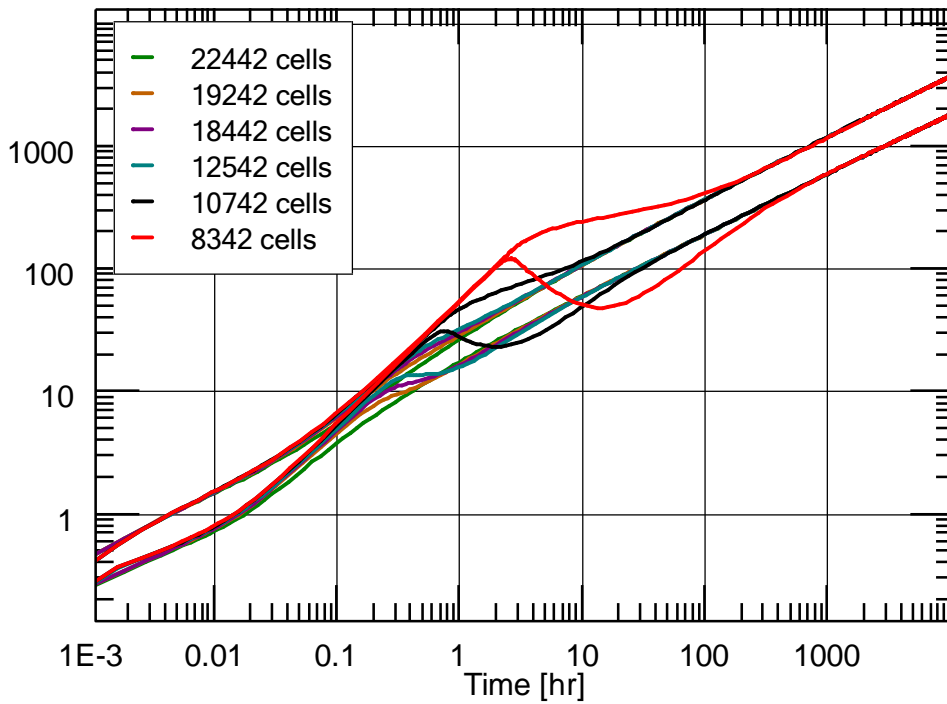*Figure 20 – Numerical forecasts for various upscaling levels*

Figure 21 – Transient numerical results for various upscaling levels

In [3], the time scale resolution of a simulation was investigated as a function of the coarsening level. The conclusion was that the size of the first grid cells (i.e. the cells close to the well or the fractures) may be chosen as a simple function of the investigation radius r, r being evaluated at the desired time resolution Δt.

$$r = \sqrt{\frac{k}{\phi \cdot \mu \cdot ct} \Delta t}$$

Above, k and ϕ are the porosity and permeability of the formation, μ is the fluid viscosity and ct is the total compressibility of the system.

We implemented this solution, taking half the investigation radius as the guess for the size of first cells. As can be seen from Figure 22, the results are quite consistent with the expectations.
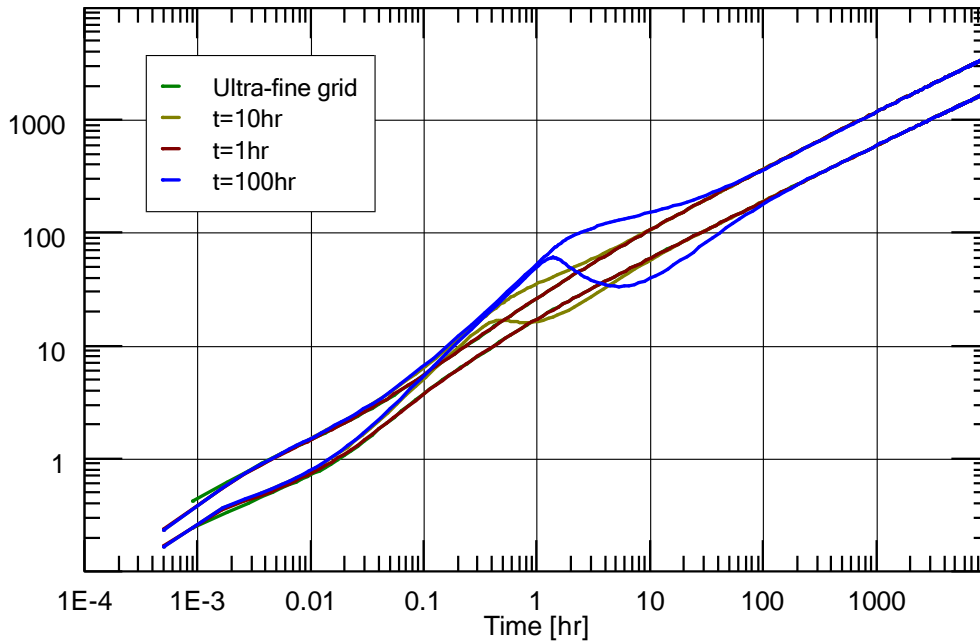

Figure 22 – Transient numerical results for various 'time resolution' choices,
with the automatic grid setting procedure – Linear PVT

One can notice that the curve obtained with the 1hr choice for the resolution even matched the ultrafine grid much earlier. This is because we want to ensure the conformity of fine and coarse grids. As a consequence, we do not have full flexibility on the first cell size, and the safest choice is taken. In this example, the finest grid contained 22442 cells, against 13742 cells for the 1hr resolution grid. The 100hr resolution grid involved 9542 cells.

These very robust results were obtained because the PVT used was linear. If we use a real, non-linear gas PVT and produce with a large pressure drop (from 5000 to 250 psi), the results are still qualitatively acceptable. However, the effective resolution of the simulation is somewhat lower than expected (Figure 23). This can be explained by the fact that the compressibility and viscosity of the fluid change significantly within the space occupied by the first cells. This effect cannot be corrected by the upstream scheme. Hence, the pressure at which compressibility and viscosity are evaluated when deriving the investigation radius should be carefully chosen, as some average values are not sufficient. As shown on Figure 23, the consequences are not dramatic with gas, even with a large pressure drop. When dealing with shale oil, however, one should ensure that the viscosity of the oil does not encounter severe variation within the pressure range corresponding to the first cells, otherwise the automatic refinement may not be suited, and even the cumulative may start deviating from the fine simulation.

In this study, we limited our analysis to very simple assumptions regarding the geometry of the fractures. For this reason, we didn't encounter any relevant inaccuracy problem associated with the coexistence of gridblocks of very different volumes (fracture vs. matrix blocks). This, however, may become more problematic when we extend this work to the simulation of natural networks of fractures [11]. In this case, other simple quality control indicators may have to be derived.
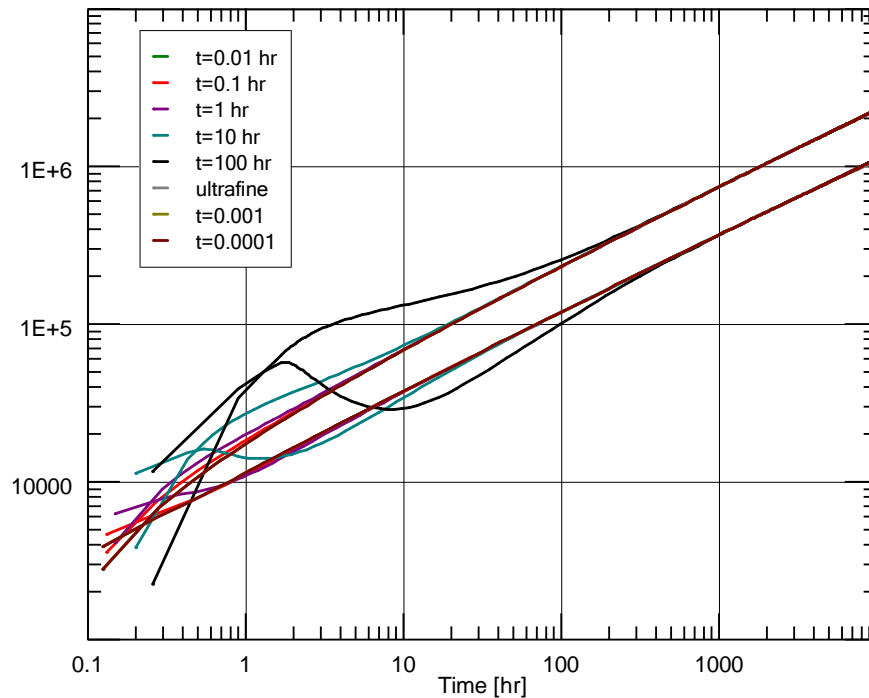
*Figure 23 – Transient numerical results for various 'time resolution' choices,
with the automatic grid setting procedure – Non-linear gas PVT*

Conclusions

Specific transmissibility derivations have been developed to address the production of multi-fractured horizontal wells in low-permeability formations. New transmissibilities are shown to improve the coherency between analytical and numerical production cumulatives, compared to the standard, linear case. It should be noticed, however, that these corrections assume high fracture permeability compared to the matrix.

When the matrix permeability is very low, transients last much longer than in the case of conventional permeability. As a consequence, for transient analysis, the size of the grid must be carefully chosen in order to account for the expected effective resolution of the simulation. An automatic grid refinement procedure has been implemented, which depends on the investigation radius at the desired resolution time scale. This process is shown to be quite robust, as long as non-linear PVT effects within the first cell are not too strong.

The proposed solutions are shown to significantly reduce numerical errors linked to the low-permeability, transient context. These initial errors can be shown to be in the same range as the uncertainty due to physical parameters in some real cases [2]. Before history matching real data, such validation hence seems essential to avoid using purely effective physical parameter values in order to simply compensate for strong numerical effects.

Acknowledgement

References

[1] Houzé, O., Tauzin, E., Artus V., Larsen, L. (2010) *The Analysis of Dynamic Data in Shale Gas Reservoirs – Part 1*. Available at: http://www.kappaeng.com/downloads/shale_gas.

[2] Houzé, O., Trin, S. and Tauzin, E. (2010) *The Analysis of Dynamic Data in Shale Gas Reservoirs – Part 2*. Available at: http://www.kappaeng.com/downloads/shale_gas.

[3] Molinari, D. (2010) *Optimization of Near-Well Upscaling in Voronoi Grids*, MSc Thesis, Politecnico di Torino

[4] Lee, S.H. (1989) *Analysis of Productivity of an Inclined Well and Its Implication for Finite-Difference Reservoir Simulation*, SPEPE, 173-180.

[5] Lee, S.H., Milliken, W.J. (1993) *The Productivity Index of an Inclined Well in Finite-Difference Reservoir Simulation*, SPE 25247, 12th SPE Symposium on reservoir Simulation, New Orleans, Feb. 28-March 3.

[6] Ding, Y. (1996) *Modeling of Fracture Wells in Reservoir Simulation*, SPE 36668, 1996 SPE Annual Technical Conference & Exhibition, Denver, Colorado, U.S.A., October 6-9.

[7] Ding, Y. (1995) *A Generalized 3D Well Model for Reservoir Simulation*, SPE 30724, 1995 SPE Annual Technical Conference & Exhibition, Dallas, U.S.A., October 22-25.

[8] Ozkan, E., Raghavan, R. (1991) *New Solutions for Well-Test Analysis Problems: Part 1 – Analytical Considerations*. SPE Formation Evaluation.

[9] Ding, Y. (1995) *Scaling-Up in the Vicinity of Wells in Heterogeneous Field*, SPE 29137, 13th SPE Symposium on reservoir Simulation, San Antonio, Texas, February 12-15.

[10] Macarenhas, O., Durlofsky, L. (2000) *Coarse Scale Simulation of Horizontal Wells in Heterogeneous Reservoirs*, JPSE, 25:135-147.

[11] Landereau, P., Noetinger, B., Quintard, M. (2001) *Quasi-steady two-equation models for diffusive transport in fractured porous media: large-scale properties for densely fractured systems*, Advances in Water Resources 24 : 863-876.

Appendix A. Unitary solutions

3D Segment source solution with linearly distributed source:

Considering a source distribution of the form $\lambda(s) = \alpha \cdot |s| + \beta$, the potential due to a segment source of length 2L is:

$$\phi(r,z) = \int_{-L}^{L} \frac{\alpha \cdot |s| + \beta}{\sqrt{(z-s)^2 + r^2}} \, ds$$

After integration we get:

$$\phi(r,z) = \alpha \cdot \left(\sqrt{r^2 + (L-z)^2} + \sqrt{r^2 + (L+z)^2} + 2\sqrt{r^2 + z^2} \right)$$

$$+ \alpha \cdot z \cdot Log\left(\frac{\left[\sqrt{r^2 + (L-z)^2} + (L-z) \right] \cdot \left[\sqrt{r^2 + (L+z)^2} + (L+z) \right]}{\left(\sqrt{r^2 + z^2} - z \right)^2} \right)$$

$$+ \beta \cdot Log\left(\frac{\sqrt{r^2 + (z-L)^2} - (z-L)}{\sqrt{r^2 + (z+L)^2} - (z+L)} \right)$$

Further considering uniform source distribution, $\lambda(s) = 1$, the solution simplifies to

$$\phi_u^{Seg}(M,F,L,\theta,\psi) = Log\left(\frac{\sqrt{r^2 + (z-L)^2} - (z-L)}{\sqrt{r^2 + (z+L)^2} - (z+L)} \right)$$

In this case one can also express analytically the gradient $\nabla \phi_u^{Seg}(M,F,L,\theta,\psi)$.

3D panel source solution with linearly distributed source:

Considering a source distribution along the panel length of the form $\lambda(s) = \alpha \cdot |s| + \beta$, the potential due to a rectangular source of length 2L and height 2H is:

$$\phi(r,z,H) = \delta(r,z,H,h1) - \delta(r,z,H,h0)$$

$$\delta(r,z,H,h) = \alpha \frac{h}{2}(g_1 + g_2 - 2g_z) + Log(2(g_1 + h)) \cdot \left[\frac{\alpha}{2}(R^2 + b_1^2) - b_1 \cdot (\alpha \cdot z + \beta) \right]$$

$$+ Log(2(g_2 + h)) \cdot \left[\frac{\alpha}{2}(R^2 + b_2^2) - b_2 \cdot (\alpha \cdot z - \beta) \right] - Log(2(g_z + h)) \cdot \alpha(R^2 - z^2)$$

$$+ h \cdot \left[(\alpha \cdot z + \beta) \cdot Log(g_1 - b_1) + (\alpha \cdot z - \beta) \cdot Log(g_2 - b_2) - 2\alpha \cdot z \cdot Log(g_z - z) \right]$$

$$+ R \cdot \left[(\alpha \cdot z + \beta) \cdot \tan^{-1}(\frac{h \cdot b_1}{R \cdot g_1}) + (\alpha \cdot z - \beta) \cdot \tan^{-1}(\frac{h \cdot b_2}{R \cdot g_2}) - 2\alpha \cdot z \cdot \tan^{-1}(\frac{h \cdot z}{R \cdot g_z}) \right]$$

$$\text{where} \begin{cases} b_1 = z - L & g_1 = \sqrt{h^2 + b_1^2 + R^2} \\ b_2 = z + L & g_2 = \sqrt{h^2 + b_2^2 + R^2} \\ & g_z = \sqrt{h^2 + z^2 + R^2} \end{cases}$$

Some special cases of interest can be derived from there, the uniform point source distribution, $\lambda(s) = 1$ is readily given in Cartesian coordinates as:

$$\phi_u^{rec}(M, F, L, H, \theta) = -b_1 \cdot Log \frac{g_1(z+H) + (z+H)}{g_1(z-H) + (z-H)} + b_2 \cdot Log \frac{g_2(z+H) + (z+H)}{g_2(z-H) + (z-H)}$$

$$+ (z+H) \cdot Log \frac{g_1(z+H) - b_1}{g_2(z+H) - b_2} - (z-H) \cdot Log \frac{g_1(z-H) - b_1}{g_2(z-H) - b_2}$$

$$+ R \cdot \left[\tan^{-1}(\frac{b_1(z+H)}{Rg_1(z+H)}) - \tan^{-1}(\frac{b_1(z-H)}{Rg_1(z-H)}) - \tan^{-1}(\frac{b_2(z+H)}{Rg_2(z+H)}) + \tan^{-1}(\frac{b_2(z-H)}{Rg_2(z-H)}) \right]$$

$$b_1 = x\frac{dx}{L} + y\frac{dy}{L} - L \qquad g_1(h) = \sqrt{h^2 + (x+dx)^2 + (y+dy)^2} \qquad R = y\frac{dx}{L} - x\frac{dy}{L}$$

$$b_2 = x\frac{dx}{L} + y\frac{dy}{L} + L \qquad g_2(h) = \sqrt{h^2 + (x-dx)^2 + (y-dy)^2} \qquad dx = L\cos\theta, dy = L\sin\theta$$

$$[x, y, z] = M - F, \text{ F the panel centre.}$$